# Enhanced Photocatalytic Activity of Hybrid rGO@TiO$_2$/CN Nanocomposite for Organic Pollutant Degradation under Solar Light Irradiation

**Martina Kocijan** [1,*] **, Lidija Ćurković** [1,*] **, Tina Radošević** [2] **and Matejka Podlogar** [2,3,*]

[1] Department of Materials, Faculty of Mechanical Engineering and Naval Architecture, University of Zagreb, Ivana Lučića 5, 10000 Zagreb, Croatia
[2] Department for Nanostructured Materials, Jožef Stefan Institute, Jamova Cesta 39, SI-1000 Ljubljana, Slovenia; tina.radosevic@ijs.si
[3] Faculty of Chemistry and Chemical Technology, University of Ljubljana, Večna Pot 113, SI-1000 Ljubljana, Slovenia
* Correspondence: martina.kocijan@fsb.hr (M.K.); lidija.curkovic@fsb.hr (L.Ć.); matejka.podlogar@ijs.si (M.P.); Tel.: +385-16168362 (M.K.); +385-16168183 (L.Ć.); +386-14473818 (M.P.)

**Abstract:** The three-component hybrid (rGO/TiO$_2$/CN) nanocomposite was prepared in order to enhance the photocatalytic properties of anatase TiO$_2$ nanoparticles (NPs) under solar-like irradiation. The rGO/TiO$_2$/CN was prepared in a mixture of the reduced graphene oxide (rGO, 8 wt%), anatase TiO$_2$ nanoparticles (NPs), and graphitic carbon nitride (g-C$_3$N$_4$, 16 wt%). It was self-assembled through the one-step hydrothermal method, followed by an annealing process. The photocatalyst was thoroughly characterized by means of X-ray diffraction (XRD), X-ray photoelectron spectroscopy (XPS), Fourier transform infrared spectroscopy (FTIR), scanning electron microscopy (SEM), transmission electron microscopy (TEM), the Brunauer-Emmett-Teller (BET) nitrogen adsorption/desorption technique and UV-Vis diffuse reflectance spectroscopy (DRS). The photocatalytic activity of the TiO$_2$, TiO$_2$/rGO, TiO$_2$/CN and hybrid rGO/TiO$_2$/CN nanocomposite was studied through the degradation of a rhodamine B (RhB) aqueous solution under solar-like irradiation. The results showed that the highest photocatalytic activity was achieved by the rGO/TiO$_2$/CN mixture, which can be attributed to the synergistic effect of the incorporation of both rGO and g-C$_3$N$_4$ with TiO$_2$. Further, the influence of the pH value of the RhB dye aqueous solution and different water matrix (Milli-Q, tap, and alkaline water) on the photocatalytic efficiency of the rGO/TiO$_2$/CN nanocomposite was examined. In addition, a recycle test was performed for hybrid rGO@TiO$_2$/CN to investigate the effectiveness of the photodegradation of RhB dye in three successive cycles. The conducted results indicate that the pH value of RhB dye aqueous solution and water matrices play an important role in the photocatalytic degradation rate.

**Keywords:** graphitic carbon nitride; reduced graphene oxide; hydrothermal synthesis; hybrid; photocatalysis; rhodamine B; solar-like irradiation; water matrix

## 1. Introduction

The presence of micropollutants on a large scale, particularly in virtually every aquatic ecosystem, has become a major problem. The widespread presence of man-made products, such as pharmaceuticals, dyes, pesticides, plastics, etc., are being detected daily, and investigation into their damaging impact on the biosphere and even human health do not show any positive aspects either. Pollution reaches the environment by different pathways, most abundantly through wastewater treatment [1,2], where currently employed wastewater treatment plants (WWTP) proved ineffective in the decomposition of harmful complexes. Given the global significance of clean water resources, new processing solutions of wastewater are required. In order to meet today's requirements and quickly introduce new technologies, solutions must be highly efficient, inexpensive and easily up-scalable.

In the field of remediation and the environmental protection of water systems, photocatalysis has attracted a lot of attention in recent years. A seemingly effective approach for this global problem employs advanced oxidation processes (AOPs) in the presence of a catalyst. The term AOP is reserved for a highly effective purification reaction in water, where the production of hydroxyl radicals (HO$^\bullet$) directly assists the decomposition of harmful organic micropollutants [3,4].

As a catalyst, titanium dioxide (TiO$_2$) was employed already very early; however, its photocatalytic application is limited due to the high recombination rate of photogenerated charge carriers and efficiency for photodegradation under abundant sunlight. The latter is due to TiO$_2$'s wide bandgap energy of 3.2 eV, which makes merely 5% of the sunlight energy effective for the reaction [5]. Given the importance of water remediation and in order to employ this fascinating, cheap, and harmless compound in other applications, many strategies have been implemented [6]. Tuning the band gap or reducing the recombination rate of the semiconductor by ion doping has been a known technique for decades. Today, catalytic limitations are being overcome by producing complex nanostructures where TiO$_2$ is coupled with metal or non-metal elements [7,8]. In these composites, heterostructures are introduced, which effectively tailor the bandgap width or recombination rate of electron-hole pairs. Such TiO$_2$-based nanocomposites have been successfully fabricated and showed enhanced photocatalytic activity shifted into the visible, e.g., sunlight range [9]. The combination of more components into the system to reduce the bandgap width, however, reduce overall catalytic activity in comparison to a single bandgap excitation, and to avoid this pitfall, so-called Z-scheme photocatalytic systems are being considered lately [10]. This photocatalytic reaction can facilely be realized by introducing a metal sink into a two-semiconductor heterojunction, by using noble metal nanoparticles, for example [11]. Very promising and mostly cheaper, however, are composites of graphene oxide/TiO$_2$/graphitic carbon nitride [5,12,13].

Graphene-based materials are attractive and well covered throughout the literature [14]. Their unique 2D structure of covalently bonded carbon atoms into a honeycomb-like lattice makes them mechanically strong and conductive, and because only a single atomic layer can be stabilized, they have a huge surface area, which gives a high aspect ratio between the junctions and bulk components. Not much thicker are graphene oxide (GO) and reduced graphene oxide (rGO) [15], two-dimensional structures with similar high mechanical strength, superb electron mobility, and great specific surface area. In the catalytic process, a graphene-based material, more commonly (rGO), serves as an electron sink, which in addition also decreases the recombination rates of the semiconductor [16,17]. The rGO/TiO$_2$ nanocomposites can easily be prepared by the sol-gel and hydrothermal method, with simultaneous TiO$_2$ growth and GO reduction to rGO [18,19].

Graphitic carbon nitride (*g*-C$_3$N$_4$), which is also added to the rGO/TiO$_2$ composite, is a two-dimensional metal-free polymeric semiconductor. The *g*-C$_3$N$_4$ with s-triazine ring structure has been of interest to researchers due to its chemical, thermal, photochemical, and physical stability, as well as for its low bandgap energy of 2.7 eV [20]. Furthermore, the synthesis of *g*-C$_3$N$_4$ by the thermal treatment of nitrogen-rich precursors such as urea, dicyandiamide, melamine, and cyanamide [21] is cheap and simple. On the other hand, the main disadvantages, such as the fast recombination of photoinduced electron-hole pairs, renders its usefulness as a single photocatalyst [22].

The preparation of a three-component hybrid (rGO/TiO$_2$/CN) photocatalyst has been used for different photocatalytic reactions [5,12,13,23]. However, in our opinion, many more experiments will have to be performed to explore the full potential of this exciting new material. Among them are two areas, namely, different synthesis routes and the investigation of photocatalytic performances and the degradation rate of other micropollutants.

Herein, the study proposes a strategy of combination anatase TiO$_2$ nanoparticles with reduced graphene oxide materials and *g*-C$_3$N$_4$ nanoparticles for generating a three-component rGO@TiO$_2$/CN hybrid. Considering that the synthesis process should be economic and eco-friendly as well as highly efficient, a simple hydrothermal method fol-

lowed by calcination treatment is proposed. The compositional, structural, morphological, and optical properties and specific surface area of the prepared materials were characterized by Fourier transform infrared spectroscopy (FTIR), Raman spectroscopy, X-ray diffraction (XRD), X-ray photoelectron spectroscopy (XPS), scanning electron microscopy (SEM), transmission electron microscopy (TEM), the Brunauer-Emmett-Teller (BET) nitrogen adsorption/desorption technique, and UV-Vis diffuse reflectance spectroscopy (DRS). Furthermore, the photocatalytic ability of prepared $TiO_2$ nanoparticles, $TiO_2$/rGO and $TiO_2$/CN nanocomposites, and rGO@$TiO_2$/CN hybrid material was monitored by the photodegradation of rhodamine B (RhB) dye. This complex and persistent pollutant is frequently found in the environment, and the presented study exploits an easily applicable process for decomposition in an aqueous medium under solar-like irradiation. The water matrix effect (Milli-Q water, tap water, and alkaline water) and the impact of the pH value of Milli-Q water on photodecomposition of RhB dye, which are known to have an effect on the degradation, were also examined. The efficiency of the photocatalytic activity of the prepared rGO/$TiO_2$/CN hybrid material was also investigated in repeated photocatalytic cycles.

## 2. Results and Discussion

### 2.1. Characterization

Raman and FTIR analyses were used to identify the chemical bonding in the synthetized photocatalysts. Figure 1A shows the FTIR spectra of the prepared GO, rGO, and $g$-$C_3N_4$ samples. The GO sample shows three characteristic absorption peaks in 1721, 1041, and 1381 cm$^{-1}$ attributed to several oxygen functional groups, i.e., C=O and C-O stretching, and C-OH bending. The stretching vibration at 1225 cm$^{-1}$ is assigned to the C-O-C of the epoxy groups. The broad stretching vibration band of the hydroxyl group, O-H, associated with absorbed water molecules and alcohol groups, is represented as a broad peak at 3380 cm$^{-1}$. Typical absorption peaks of GO disappear in the rGO spectrum. There, the absorption peak at 1617 cm$^{-1}$ is assigned to the skeleton vibration of less-oxidized graphitic materials, C=C. Comparison between the rGO spectrum and the GO spectrum shows that the reduction of GO by thermal treatment was significant. In the FTIR spectrum of the $g$-$C_3N_4$ sample, several strong peaks were observed in the 1200–1650 cm$^{-1}$ region. Typical stretching vibrations of C-N heterocycles are represented at 1217, 1315, 1395, and 1452 cm$^{-1}$. The two bands appeared at 1541 and 1633 cm$^{-1}$, related to the stretching vibrations of C=N heterocycles, while the peaks located at 885 and 804 cm$^{-1}$ arose from the characteristic breathing mode of tri-s-triazine rings units. All are characteristic for $g$-$C_3N_4$ material. The extra vibrational region between 3000–3300 cm$^{-1}$, although not directly related to the $g$-$C_3N_4$ structure, is commonly found in this compound [5,24], and can be associated with $H_2O$ absorption and possible N-H bonds at the surface. Figure 1B shows characteristic functional vibrations of FTIR spectra of the prepared pure $TiO_2$ nanoparticles, $TiO_2$/rGO, $TiO_2$/CN nanocomposites, and the rGO@$TiO_2$/CN hybrid photocatalyst.

Raman spectra of pure $TiO_2$ nanoparticles, GO, thermally treated rGO, and the prepared rGO@$TiO_2$/CN hybrid material are displayed in Figure 2A. The typical bands of anatase $TiO_2$ are located at 147, 398, 517, and 641 cm$^{-1}$, which are attributed to the $Eg_{(1)}$, $B_{1g}$, $A_{1g} + B_{1g}$, and $E_{g(2)}$, respectively. The Raman spectrum of synthesized GO showed two typical peaks at the wavenumber of 1356 cm$^{-1}$ and 1607 cm$^{-1}$, which corresponds to the D and G bands. The D band is associated with the in-plane $sp^3$ defects, while the G band represents in-plane vibrations of ordered $sp^2$-bonded carbon atoms in a two-dimensional hexagonal lattice. The D and G bands, after the hydrothermal reduction process, are shifted to the lower wavenumber at 1336 cm$^{-1}$ and 1591 cm$^{-1}$. In the case of rGO, the D band got slightly larger with the reduction process, which increased the level of defects in the material, while the shifted G band indicates the re-graphitization process [25]. The Raman spectrum of the rGO@$TiO_2$/CN hybrid sample contained four characteristic bands of anatase phase of $TiO_2$ and two typical bands of rGO (D and G) The D and G bands in the prepared rGO@$TiO_2$/CN sample were found in the unchanged position as in the rGO

sample, which suggests a reduction level similar to the pure GO reduction. As shown Raman spectrum of $g$-C$_3$N$_4$, a broad peak was observed between 1200–1800 cm$^{-1}$, which is similar to other reports [13,26]. Although two characteristic peaks, corresponding to D and G bands, should be resolved in this region, the obtained spectrum did not clearly express this feature. This was either because the excitation energy (633 nm excitation) was not optimal for the material [27], which could include defects, or because it was less crystalline. The intensity ratios of the D and G bands ($I_D/I_G$), specifically, show the concentration of the sp$^3$ hybridized defects with respect to the sp$^2$-hybridized graphene domains. The hydrothermally prepared hybrid sample shows a higher intensity ratio ($I_D/I_G$ = 1.10) in comparison with the synthesized GO sample ($I_D/I_G$ = 1.02). According to [5], this suggests an interplay between TiO$_2$ intercalation and variation in defect concentration. Thus, Raman results better prove chemical interaction between graphene material and TiO$_2$ nanoparticles.
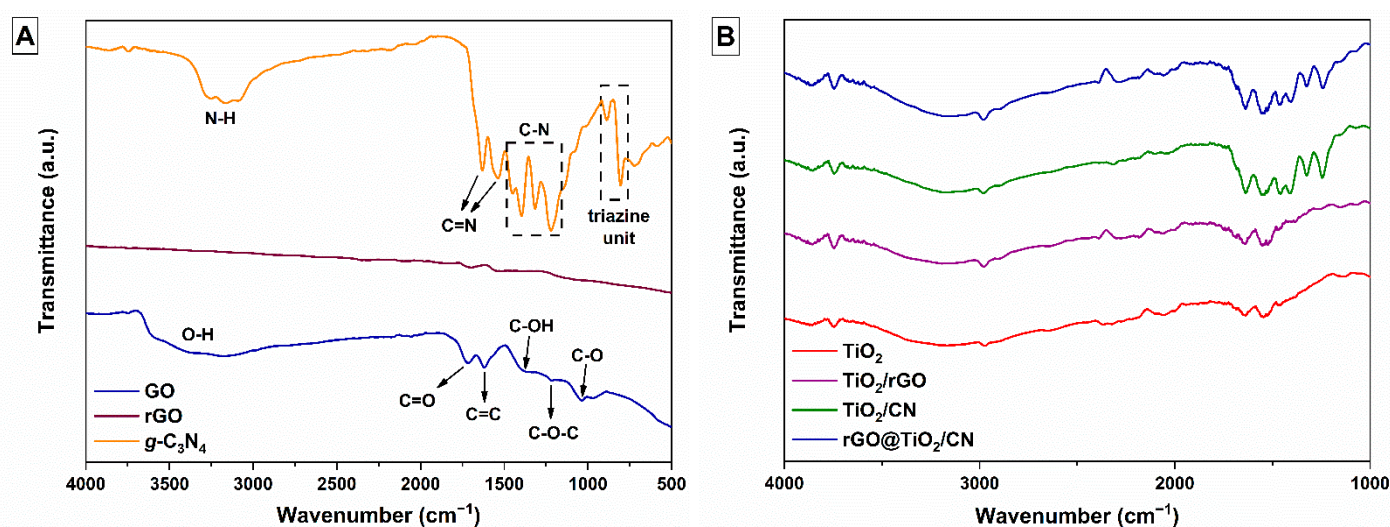


**Figure 1.** (**A**) FTIR spectra of as-prepared GO, rGO, and $g$-C$_3$N$_4$ materials and (**B**) pure TiO$_2$ nanoparticles, TiO$_2$/rGO, TiO$_2$/CN nanocomposites, and rGO@TiO$_2$/CN hybrid photocatalyst.
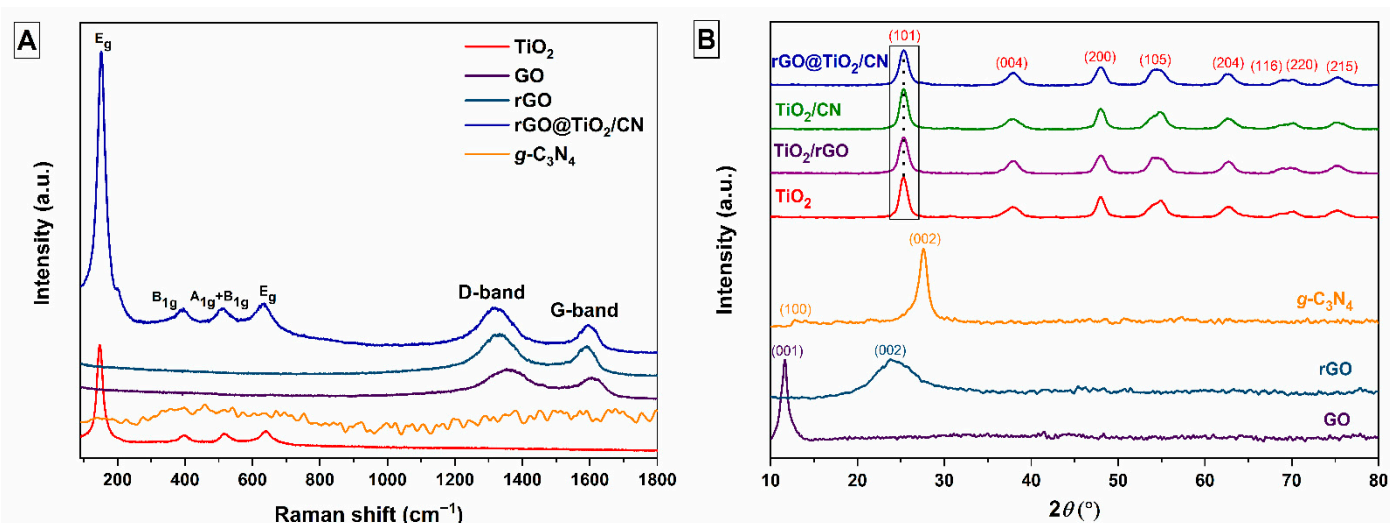


**Figure 2.** (**A**) Raman spectra of TiO$_2$, GO, rGO, $g$-C$_3$N$_4$, and rGO@TiO$_2$/CN nanocomposite, and (**B**) XRD patterns of the prepared materials.

Figure 2B shows the X-ray powder diffraction pattern of the prepared GO, rGO, $g$-$C_3N_4$, pure $TiO_2$ nanoparticles, $TiO_2$/rGO and $TiO_2$/CN nanocomposites, and rGO@$TiO_2$/CN hybrid samples. The GO pattern shows the strong diffraction peak at $2\theta$ = 11.5° (001), which corresponds to an interlayer spacing of 0.76 nm and indicates the presence of oxygen functional groups in the GO sample [28]. In the rGO pattern, the broad diffraction peak is located at $2\theta$ = 23.8° (002), which corresponds to an interlayer spacing of 0.74 nm. The decreased interlayer confirms the successful reduction of GO to rGO by applied hydrothermal treatment [19]. The $g$-$C_3N_4$ pattern contains two characteristic diffraction peaks according to JCPDS card no. 87-1526. The weaker peak located at $2\theta$ = 12.8° (100) corresponds to an in-plane structural repeating of tri-s-triazine units and represents an interlayer spacing value of 0.69 nm. The sharp diffraction peak presented at $2\theta$ = 27.5° (002) corresponds to the interlayer stacking of the conjugated aromatic segments with an interlayer spacing of 0.32 nm [20]. The nanoparticles synthesized by the simple hydrothermal method showed a crystalline nature, with $2\theta$ peaks lying at 25.29° (101), 37.96° (004), 48.03° (200), 54.89° (105), 62.74° (204), 68.78° (116), 70.23° (220), and 75.35° (215). According to JCPDS card no. 21-1272, all the diffraction peaks of $TiO_2$ sample can be indexed to a pure anatase phase. These peaks are also observed in the prepared $TiO_2$/rGO, $TiO_2$/CN, and rGO@$TiO_2$/CN samples. Furthermore, in all the composite mixtures, XRD analysis failed to detect clear $g$-$C_3N_4$ or rGO presence, mostly due to a low mass percentage of the later, but also because carbon-based compounds lack long range order, which would be similar to $TiO_2$. Using the Scherrer equation, the crystalline domain size of the $TiO_2$ particle for all prepared samples was also estimated. The obtained crystallite size using (101) peak and a shape factor of 0.9 showed similar values around 7 nm (Table 1) for all samples.

**Table 1.** Calculated crystallite size ($D$, nm) of $TiO_2$ samples using the Scherrer equation.

| Sample ID | $D$, nm |
|:---:|:---:|
| $TiO_2$ | 7.6 |
| $TiO_2$/rGO | 6.8 |
| $TiO_2$/CN | 7.5 |
| rGO@$TiO_2$/CN | 6.7 |

As revealed by the SEM (Figure 3A), pure $TiO_2$ crystals precipitated in the form of spheres. It was found that the particle size was smaller than 10 nm, which is consistent with the calculated crystallite size of 7.6 nm (Table 1). The SEM analysis of pure rGO and $g$-$C_3N_4$ materials pointed out to their known high specific surface area (Figure 3B,C), while imaging of the composite $TiO_2$/rGO, $TiO_2$/CN, and rGO@$TiO_2$/CN composite samples revealed similar $TiO_2$ crystals precipitated at the surface of the hybrid system (Figure 3D–F). Obviously, bigger aggregates in the composite samples arise most probably during the drying sequence and as is shown later, do not diminish degradation process. Figure 4 shows the TEM image of the rGO@$TiO_2$/CN hybrid material, where the $TiO_2$ component is undoubtedly resolved, while carbon containing compounds are not so clear. However, the sheet of rGO and fiber-like $g$-$C_3N_4$ are obviously present, and EDS shows Ti, O, C, and N over the region of this hybrid material. The average size of anatase $TiO_2$ nanoparticles is around 6 nm.

The specific surface area of the rGO@$TiO_2$/CN hybrid material was determined by the Brauner-Emmett-Teller (BET) method, and it was 185.82 $m^2$/g. The obtained result is higher than to the literature findings, based on similar preparation procedures for the rGO@$TiO_2$/CN hybrid [29].
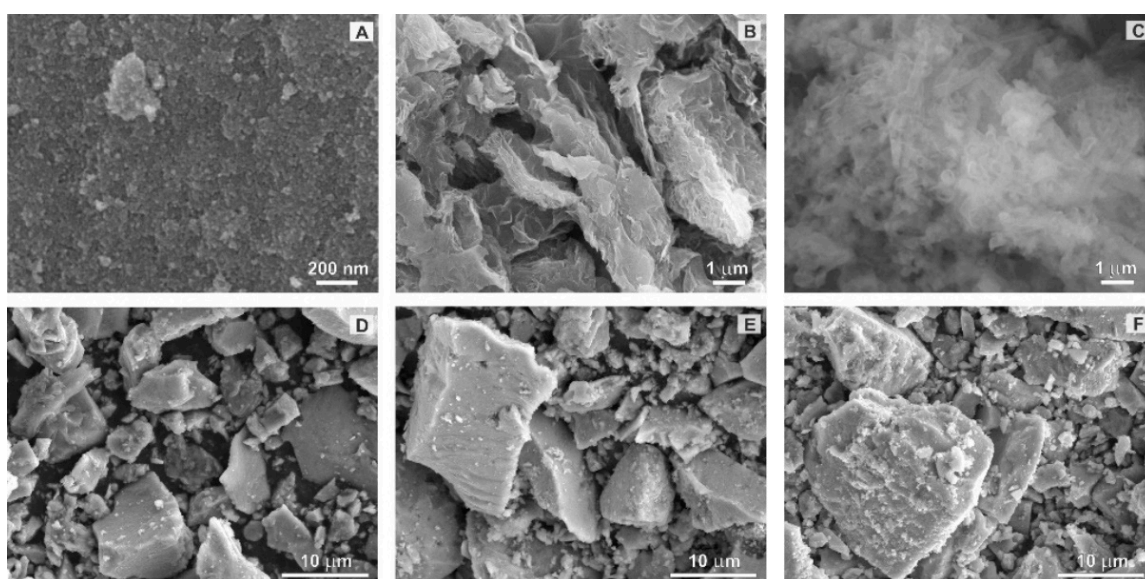
**Figure 3.** SEM images of (**A**) pure $TiO_2$ nanoparticles, (**B**) rGO, (**C**) *g*-$C_3N_4$, (**D**) $TiO_2$/rGO, (**E**) $TiO_2$/CN, and (**F**) rGO@$TiO_2$/CN.
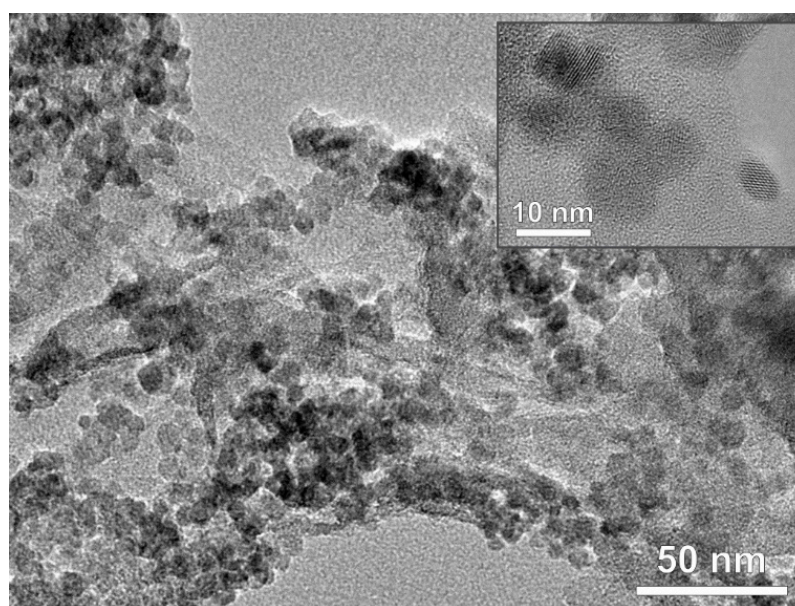


**Figure 4.** TEM image of rGO@$TiO_2$/CN nanocomposite and inset of anatase $TiO_2$ nanoparticles.

The surface chemical composition and oxidation state of the as-prepared rGO@$TiO_2$/CN hybrid material were determined by XPS analysis, as shown in Figure 5. Figure 5A shows the full spectrum of characterized photocatalyst; Ti, O, C, and N peaks can be observed. Moreover, the peak intensities of Ti and O elements are clearly stronger than that of C and N, which corresponds to the obtained XRD results. The high-resolution spectrum of Ti 2p is shown in Figure 5B. The Ti 2p spectrum contains two symmetric peaks centered at 465.0 eV and 459.3 eV, which correspond to the Ti $2p_{1/2}$ and Ti $2p_{3/2}$. The obtained binding energy values correspond with $Ti^{4+}$ in the $TiO_2$ chemical environments. The peak was determined at 456.7 eV, which can be attributed to the Ti-N bond due to the solid adhesion of $TiO_2$ on the *g*-$C_3N_4$ surface [18,30]. Based on this, Figure 5C shows the O 1s spectrum. The main peak is located at 530.5 eV, assigned to oxygen bonded to titanium (Ti-O-C), and a smaller peak around 531.3 eV, ordinarily attributed to hydroxyl groups in the structure of $TiO_2$. Figure 5D represents the N 1s spectrum, which can be fitted into two peaks with

binding energies centered at 399.3 eV and 400.5 eV, assigned to the sp$^2$-hybridized nitrogen atom in the C-N=C group of triazine rings and sp$^3$-hybridized tertiary nitrogen N-(C)$_3$ in the heptazine unit [5]. The peak located at 401.4 eV, attributed to the C-N-H bond, which signifies the covalent bonding between rGO and *g*-C$_3$N$_4$, was not determined [30]. As shown in Figure 5E, the C1s spectrum could be divided into four peaks. The binding energies of the observed peaks at 284.5 and 287.2 eV can be assigned to the sp$^2$-hybridized carbon atom in the C-C bond and oxygen-containing epoxy/hydroxyl groups bond in the rGO material. The observed peaks located at 285.9 eV and 288.6 eV correspond to the sp$^2$-bonded carbon in N-containing (C-N-C) and (N)$_2$-C=N in the aromatic ring of the *g*-C$_3$N$_4$ material [5,30]. Overall, the analysis of XPS results for the as-prepared rGO@TiO$_2$/CN hybrid material reveals successful interactions of *g*-C$_3$N$_4$ and rGO with TiO$_2$ nanoparticles and the pure form of the prepared hybrid sample.
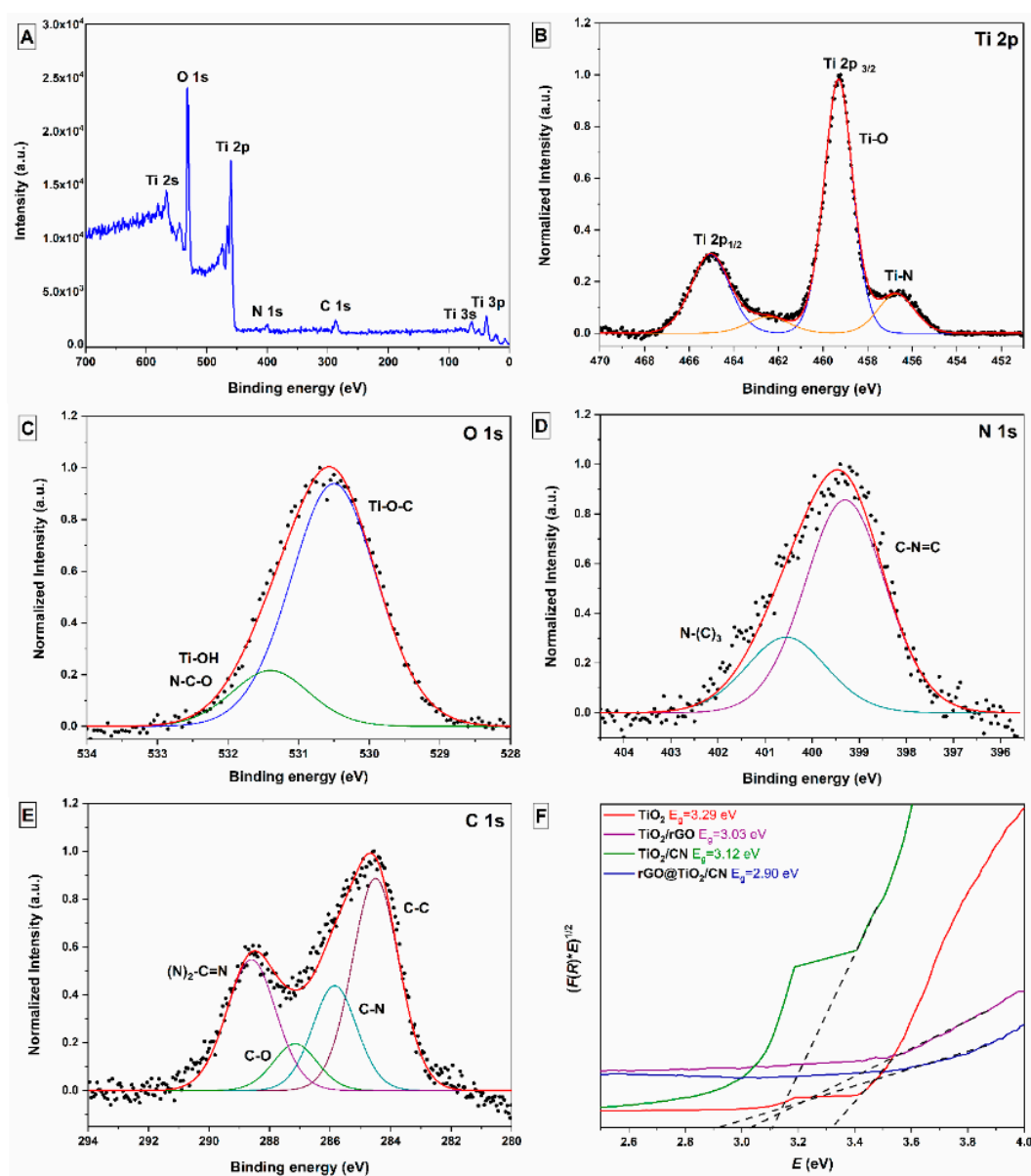


**Figure 5.** High-resolution XPS spectra of the as-prepared rGO@TiO$_2$/CN sample: (**A**) fully scanned spectrum, (**B**) Ti 2p, (**C**) O 1s, (**D**) N 1s, (**E**) C 1s, and (**F**) band gap energies (*E*$_g$) of prepared pure TiO$_2$ nanoparticles, TiO$_2$/rGO, and TiO$_2$/CN nanocomposites, and rGO@TiO$_2$/CN hybrid.

UV-Vis DRS measurements were employed to investigate the optical properties of the prepared samples, as displayed in Figure 5F. The band gap energies ($E_g$) of the prepared samples were estimated from the linear extrapolation of the Tauc's plot of the Kubelka–Munk function versus the energy of the photon using the following equation [13]:

$$\alpha h\nu = k(h\nu - E_g)^{\frac{1}{2}} \tag{1}$$

where $\alpha$, $h$, $\nu$, $k$, and $E_g$ are the optical absorption coefficient, Planck constant, photon frequency, constant of proportionality, and band gap energy, respectively. The obtained band gap energy of $TiO_2$ is 3.29 eV. After the incorporation of $TiO_2$ nanoparticles into rGO and $g$-$C_3N_4$ material, the band gap energies decrease to 3.03 and 3.12 eV for $TiO_2$/rGO and $TiO_2$/CN nanocomposites, respectively, while the hybrid rGO@$TiO_2$/CN shows an even lower band gap energy of 2.90 eV.

### 2.2. Photocatalytic Activity

To test the photocatalytic performances of the synthesized $TiO_2$ nanoparticles, $TiO_2$/rGO, $TiO_2$/CN nanocomposites, and rGO@$TiO_2$/CN hybrid material, their effectiveness to RhB dye degradation in an aqueous medium (Milli-Q water) was performed. Standard procedure was employed for a period of 75 min in the dark and 120 min under solar-like irradiation. A period of the dark adsorption was split into two parts. Firstly, the reactants were transferred in the ultrasonication bath to achieve the homogenous distribution of the RhB dye solution, then the homogenous suspension were stirred in the dark for the next 60 min to reach an adsorption-desorption equilibrium. The adsorption results and photocatalytic degradation rates are displayed in Figure 6A. After 15 min of ultrasonication bath, the small adsorption (<16%) of initial RhB dye concentration was observed for all tested photocatalysts. Furthermore, no considerable decrease in RhB dye concentration (9.3%) in Milli-Q water was observed during the stirring in the dark. The highest total absorption during the 75-min dark period was found for the prepared hybrid photocatalyst (i.e., 25.8%), which can be a consequence of adsorption on both rGO and $g$-$C_3N_4$ since both possess adsorbent properties. The smallest adsorption of 11.9% was observed for $TiO_2$, while $TiO_2$/rGO and $TiO_2$/CN exhibited 19.8% and 13.1%, respectively.
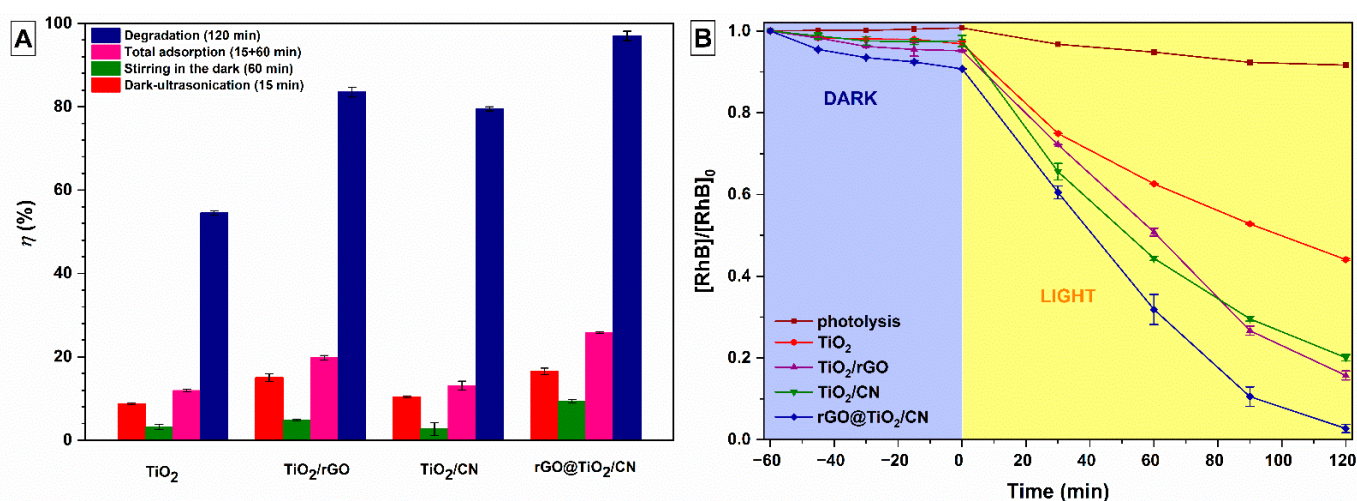


**Figure 6.** (**A**) The percentage of adsorption for RhB dye in aqueous solution (Milli-Q water) after ultrasonication (15 min)—red, stirring in the dark (60 min)—green and total dark adsorption (15 + 60 min)—pink, and photocatalytic degradation efficiency (after 120 min)—blue under solar-like irradiation. (**B**) Photocatalytic degradation of RhB aqueous solution (Milli-Q water) in the dark and under light irradiation.

The photolysis test of RhB dye in an aqueous medium was monitored and the observed result shows sensitivity to solar-like irradiation (displayed in Figure 6B). The tested nanocomposites exhibit a noticeable degradation rate, where the RhB dye degradation rate is enhanced significantly with the use of the prepared rGO@TiO$_2$/CN hybrid material. The obtained photocatalytic results clearly demonstrate that the incorporation of rGO and $g$-C$_3$N$_4$ materials in hybrid photocatalyst has a crucial effect on the photodegradation rate. The degradation rate constant $k$ (min$^{-1}$) was determined from the slope of the straight line obtained from plotting the linear regression of $-ln$ ($C_t/C_0$) versus time (not shown here), which can be directly connected to the photoactivity performances. The photocatalytic activity of all tested materials follows the first-order kinetic rate ($k$, min$^{-1}$). The obtained values of the first-order rate constant ($k$) and the photocatalytic degradation efficiency ($\eta$) decrease in the following order: rGO@TiO$_2$/CN > TiO$_2$/rGO > TiO$_2$/CN > TiO$_2$ (Table 2). Therefore, the photocatalytic efficiency of the photocatalytic degradation of RhB dye by the hybrid rGO@TiO$_2$/$g$-C$_3$N$_4$ nanocomposite at different pH values and different water environments was investigated.

**Table 2.** The values of the first-order rate constant ($k$) and efficiency ($\eta$) of RhB dye aqueous solution photodegradation by prepared photocatalysts.

| SAMPLE ID | $k \times 10^{-3}$, min$^{-1}$ | $\eta$, % |
|---|---|---|
| TiO$_2$ | 6.4 | 54.5 |
| TiO$_2$/rGO | 15.3 | 83.5 |
| TiO$_2$/CN | 13.2 | 79.5 |
| rGO@TiO$_2$/CN | 29.2 | 97.0 |

Strategies to increase the catalytic activity of two semiconductors by introducing metal mediators have been proven in a few different systems [5,9] but also for this particular system using the same components [12,13,23]. Mostly, the explanation considers the decrease in the recombination rate of the generated electron-hole pairs. Wang et al. [23] went further by also considering the change in electron band structure. In their experiments, the catalytic activity of the $g$-C$_3$N$_4$/rGO/TiO$_2$ was increased by generating point defects in this composite. Further treatment of the material in Ar/H$_2$ flow increased the performance over that of the $g$-C$_3$N$_4$/TiO$_2$ and untreated $g$-C$_3$N$_4$/rGO/TiO$_2$ for a hydrogen evolution reaction. A further increase in the catalyst performance could also be influenced by defects on the surface. In the adsorption in the dark, the TiO$_2$/rGO composite saturates adsorption below that of the TiO$_2$/CN value, (Figure 6B) which is probably a consequence of a higher defect concentration on rGO. The three-phase composite most probably has the highest number of surface defects and also the highest catalytic activity.

The influence of pH value plays an important role in the rate of photocatalytic degradation of dyes due to its effects on the charge of the catalyst surface, adsorption, certain physico-chemical properties, and potential of valence band (VB) oxidation [31]. In order to determine the influence of pH value on the degradation of RhB dye in Milli-Q water, the following pH values were investigated: 3.1, 7.4, 10.7, and 12.5, respectively. The natural pH of the RhB dye in Milli-Q water was 6.18.

In all reactions, the amount of rGO/TiO$_2$/CN catalyst (5 mg/mL) and the concentration of RhB dye (10 mg/L) in aqueous solution (Milli-Q) were kept constant. The obtained results are displayed in Figure 7 and Table 3. It can be observed that the photocatalytic degradation rate of RhB dye increased by increasing pH values. In an alkaline medium, the photodegradation rate significantly increased due to the influence of hydroxide ions (OH$^-$). On the other hand, the photodegradation rate notably decreased at lower pH, which can be ascribed to the influence of H$^+$ ions [32].
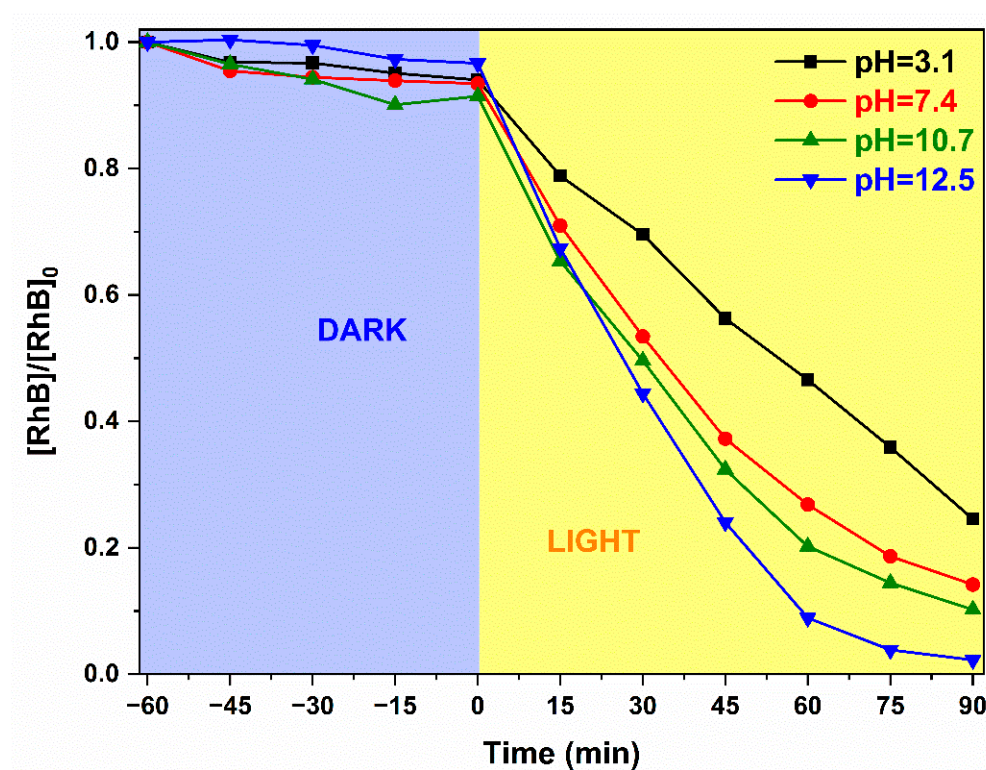
**Figure 7.** The influence of the pH value of the RhB dye solution in Milli-Q water on the photocatalytic degradation efficiency in the presence of rGO@TiO$_2$/CN hybrid as photocatalyst.

**Table 3.** Photocatalytic degradation of RhB dye in aqueous solution (Milli-Q) at different pH values.

| pH | $k \times 10^{-3}$, min$^{-1}$ | $\eta$, % |
|---|---|---|
| 3.1 | 14.3 | 73.9 |
| 7.4 | 21.5 | 84.8 |
| 10.7 | 25.0 | 88.8 |
| 12.5 | 44.3 | 97.6 |

Because the Z-scheme photocatalysis is also dependent on the water environment and pH value [9], adsorption and photocatalytic degradation rates of RhB dye in various water environments were also investigated. The obtained results for RhB dye degradation using rGO/TiO$_2$/CN in Milli-Q water, tap water, and alkaline water (Fructal) are collected in Figure 8. The adsorption efficiency of RhB on the rGO/TiO$_2$/CN nanocomposite (<8%) was not significant in all the investigated water environments. On the other hand, the significant photodegradation of RhB dye was observed in all tested samples. Furthermore, the Milli-Q water almost completely degraded the RhB dye in 120 min of solar-like irradiation, while at the end of the reaction time, 6.4%, and 8.1% of RhB dye concentrations remained in alkaline water and tap water, respectively. The degradation of RhB dye following the first-order kinetic rate is depicted in Table 4.

Various inorganic ions and organic matters can inhibit the photocatalytic degradation [29]. Present ions in water matrices can act as scavengers that may affect the degradation rate of organic pollutants. According to the obtained results of conductivity measurements (shown in Table 4), Milli-Q water, with the lowest ion concentration, outperformed alkaline and tap water, which showed significant conductivity, i.e., a higher ion concertation [33]. Although all tested water environment matrices show an effective photodegradation rate for RhB dye, Milli-Q water outperformed them all. This suggests that the optimal concertation of ions is required for optimal decomposition (Figure 8 and Table 4).
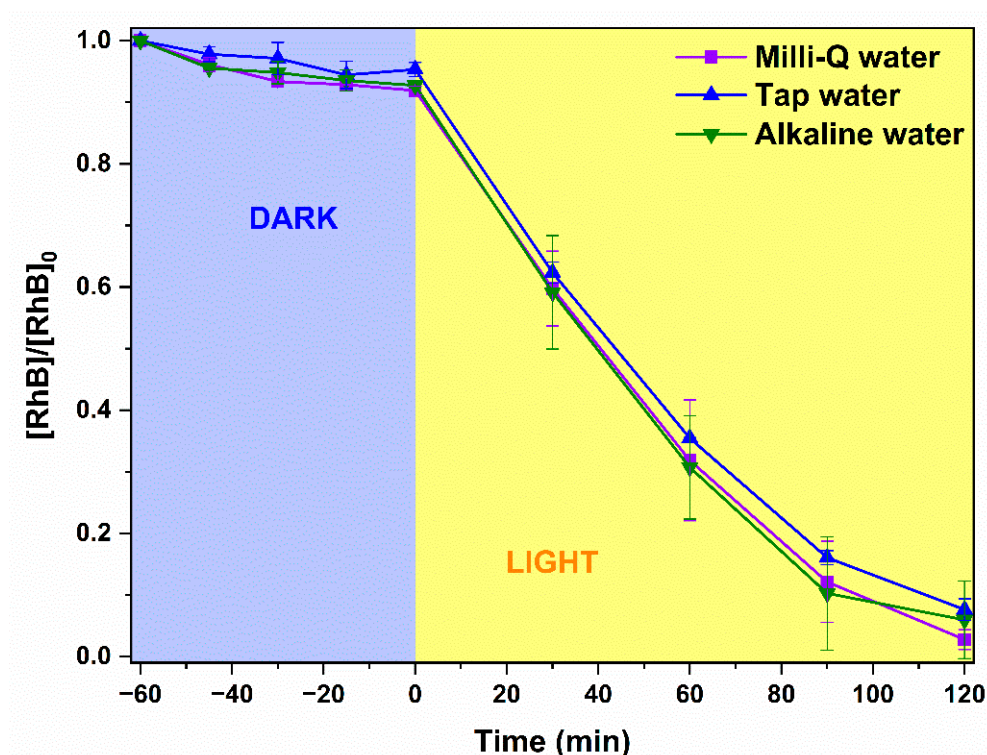
**Figure 8.** Effect of different water matrices (Milli-Q water, tap water, and alkaline water (Fructal)) on the degradation efficiency of RhB dye using rGO/TiO$_2$/CN nanocomposite photocatalyst under solar-like irradiation.

**Table 4.** The values of the first-order rate constant ($k$) and efficiency ($\eta$) of RhB dye photodegradation by rGO/TiO$_2$/CN nanocomposite photocatalyst, in different water matrix.

| SAMPLE ID | pH | Conductivity, μS/cm | $k \times 10^{-3}$, min$^{-1}$ | $\eta$, % |
|---|---|---|---|---|
| Milli-Q water | 6.18 | 0.380 | 28.7 | 97.2 |
| Alkaline water | 8.81 | 227 | 24.1 | 93.6 |
| Tap water | 7.57 | 492 | 21.3 | 91.9 |

　　　The change of pH, however, did not show this trend. Instead, the degradation rate continuously increased with pH (Figure 7) and at 12, the fastest degradation was observed. On the other hand, a high degradation rate at elevated pH values can also be ascribed to changes in the composite surface.

　　　The prepared rGO@TiO$_2$/CN hybrid photocatalyst was used for three successive photoactivity cycles to investigate reusability. The results of three successive photocatalytic cycles are displayed in Figure 9. The efficiency of dye removal was 97.2% after the first cycle, followed by 88.5% and 82.3% after the second and third cycles, respectively. Although a slight decline in the photodegradation rate could be associated with diminishing photoactivity, a small amount of photocatalyst was also lost after the successive cycle during the separation and washing process, which utilized centrifugation to recover the rGO@TiO$_2$/CN hybrid. Thus, we can safely conclude, that the rGO@TiO$_2$/CN photocatalyst can successively be reused after drying, which makes it a promising hybrid material.
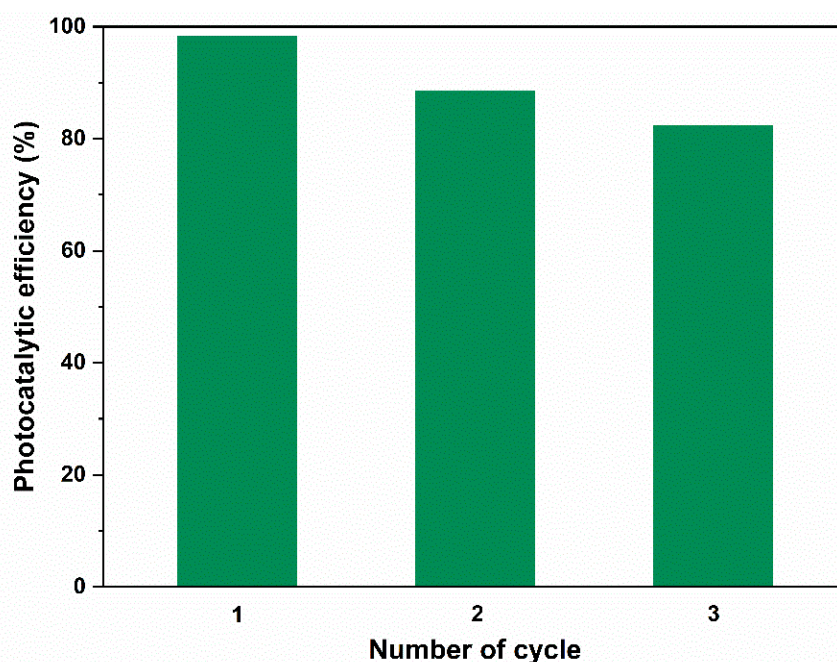
**Figure 9.** The reusability of the prepared rGO@TiO$_2$/CN hybrid in the photocatalytic degradation of RhB dye in Milli-Q water under simulated solar-like irradiation for 120 min.

## 3. Materials and Methods

### 3.1. Materials

Urea ($\geq$99%), graphite flakes ($\leq$50 μm), and titanium (IV) and isopropoxide (Ti(C$_3$H$_5$O$_{12}$)$_4$, TTIP, 97%) were purchased from Merck KGaA (Darmstadt, Germany). An *i*-propanol (C$_3$H$_7$OH) was purchased from Gram mol (Zagreb, Croatia). Acetylacetone (CH$_3$(CO)CH$_2$(CO)CH$_3$) was purchased from VWR Chemicals GmbH (Dresden, Germany). Hydrochloric acid (HCl, 37%), potassium permanganate (KMnO$_4$), sodium nitrate (NaNO$_3$), hydrogen peroxide (H$_2$O$_2$, 30% *w/v*), and rhodamine B (RhB), [9-(2-carboxyphenyl)-6-diethylamino-3-xanthenylidene]-diethylammonium chloride were purchased from Merck KGaA (Darmstadt, Germany). The ultra-pure water was produced in a LaboStar® PRO water purification system (resistivity 18.2 MΩ/cm at 24.5 °C, 0.2 μm sterile filter, Siemens). Alkaline water was received from Fructal (Ajdovščina, Slovenia).

### 3.2. Preparation of rGO@TiO$_2$/CN Photocatalyst

The bulk graphitic carbon nitride (*g*-C$_3$N$_4$) was prepared from urea. A total of 10 g of urea was put into a covered ceramic crucible in a chamber furnace (Nabertherm, Germany), it was heated up to 550 °C at a rate of 5 °C/min and left for 2 hours to dwell. Consequently, it was cooled to room temperature to obtain a light-yellow bulky *g*-C$_3$N$_4$ powder. Graphene oxide (GO) was synthesized from natural graphite flakes ($\leq$50 μm) via Hummers' method according to the previous report [18]. To prepare the nanocomposites, at first, TiO$_2$ colloidal solution was prepared in the following components and molar ratios: TTIP:PrOH:AcAc:HN = 1:35:0.63:0.015, as reported in [34]. According to the previously reported literature results [5,15], the selected amount of the synthesized GO suspension (8 wt%) and *g*-C$_3$N$_4$ nanosheets (16 wt%) was added to the prepared TiO$_2$ sol with continuous stirring for 15 min at 500 rpm. The prepared suspension was ultrasonicated for 15 min to acquire homogeneous dispersion of all added materials. The photocatalysts were synthesized by a simple one-pot hydrothermal method. The whole reaction mixture was relocated into a Teflon-lined autoclave and kept in an oven at 180 °C for 6 h. Subsequently, the precipitate was centrifuged at 3000 rpm to separate it from the supernatant, and then washed with the ethanol and distilled water, and dried at around 80 °C over the night. For comparison, pure TiO$_2$ nanoparticles, rGO/TiO$_2$ and TiO$_2$/CN nanocomposites were

also synthesized through a similar procedure with the same hydrothermal method and parameters of the synthesis. The synthesized materials were put into a crucible to anneal them at 300 °C with a heating rate of 3 °C/min and 2 h dwelling time, then cooled naturally to room temperature.

### 3.3. Photocatalysts Characterization

To provide information related to the specific functional groups, the Fourier transform infrared spectroscopy-attenuated total reflectance (FTIR-ATR, Shimadzu, Kyoto, Japan) measurements were performed in the 400–4000 cm$^{-1}$ range at room temperature. Raman spectra measurements of the prepared samples were recorded at room temperature on the Raman microscope (NT-MDT Spectra II, Moscow, Russia) using a 633 nm laser. The crystallinity phase and composition of the prepared powders were obtained by an X-ray diffractometer (X'Pert PRO high-resolution X-ray diffractometer; PANalytical B.V., Almelo, Netherlands) using CuK$\alpha$ a radiation source ($\lambda = 1.5406$ Å) at $2\theta$ ranging from 8° to 80° with step of 0.033°/100 s. A Shimadzu UV-Vis-NIR Spectrophotometer (UV-3600, Kyoto, Japan), using BaSO$_4$ as a reference, was used to measure the UV-Vis diffuse reflectance spectra (DRS). The morphology of the products was studied using a scanning electron microscope (FIB-SEM dual beam, Helios NanoLab NL650, FEI, Hillsboro, OR, USA and a transmission electron microscope (TEM, Jeol JEM-2100, Jeol Ins., Tokyo, Japan). The chemical composition and bonding were characterized by XPS in a SPECS XPS spectrometer equipped with a Phoibos MCD 100 electron analyzer and a monochromatized source of Al K$\alpha$ X-rays of 1486.74 eV. The typical pressure in the UHV chamber during analysis was in the $10-7$ Pa range. For the electron pass energy of the hemispherical electron energy analyzer of 10 eV used in the present study, the overall energy resolution was around 0.8 eV. All spectra were calibrated by the position of C 1s peak, placed at the binding energy of 284.5 eV. The XPS spectra were deconvoluted into several sets of mixed Gaussian-Lorentzian functions with Shirley background subtraction. The specific surface area was performed by the Brunauer-Emmett-Teller (BET) method with a nitrogen adsorption analyzer (Quantachrome Nova 2000e, Anton Paar QuantaTec Inc., Graz, Austria).

*d*-interplanar spacing was calculated according to the following equation [16]:

$$\frac{1}{d^2} = \frac{h^2 + k^2}{a^2} + \frac{l^2}{c^2} \tag{2}$$

where *d* represents the interplanar distance and *h*, *k* and *l* are Miller indices.

The crystalline sizes for the prepared samples were calculated using the Scherrer equation [35]:

$$D[\text{nm}] = \frac{K \times \lambda}{\beta \times \cos\theta} \tag{3}$$

where *D* is the crystallite size, *K* is a dimensionless shape factor with a value 0.9, $\lambda$ is the X-ray wavelength, 0.15406 nm, $\beta$ is the full line in width at half-maximum height of the main intensity peak in radians, and $\theta$ is the Bragg's angle in degrees.

### 3.4. Photolytic, Adsorption and Photocatalytic Experiments

To test the photocatalytic activity of the prepared nanocomposites, an aqueous RhB solution (10 mg/L) was irradiated using Osram's Ultra Vitalux bulb as a solar-like irradiation source. The total radiation emitted by solar-like irradiation was found to be around 64 mWcm$^{-2}$, as determined by specification from the lightbulb supplier. The bulb was kept 15 cm away from the solution in the beaker. First the photolysis of the RhB aqueous solution was investigated during the solar light irradiation of the RhB aqueous solution for 120 min. After that, adsorption and photocatalytic experiments were performed by the dispersion of 5 mg of the prepared photocatalysts in 10 mL of RhB solution. Before the light turned on, a dark adsorption was performed for 60 min in order to achieve an adsorption-desorption equilibrium. The magnetic stirrer was continuously turned on during the tests. The tested suspensions were sampled in the regular interval times and

the photocatalyst was removed from the suspension by centrifugation in a mini centrifuge (Eppendorf, Hamburg, Germany) at 13,400 rpm for 5 min. The absorbance was monitored by UV-Vis spectroscopy on a Lambda 950 UV/VIS/NIR spectrophotometer (PerkinElmer, Waltham, MA, USA) in the 400–700 nm range using quartz cuvette (Hellma Analytics, Stuttgart, Germany) with a path length of 10 mm.

The adsorption and photocatalytic degradation rates ($\eta$) were calculated using the following equation [15,30]:

$$\eta \ (\%) = \frac{A_0 - A_t}{A_0} \times 100 \tag{4}$$

where $A_0$ and $A_t$ refer to the initial absorbance and absorbance at the interval time ($t$) irradiation of the RhB dye, respectively.

Furthermore, the rate constant of the photocatalytic degradation process of the RhB dye was evaluated by the Langmuir-Hinshelwood equation [36]:

$$\ln \frac{A_0}{A_t} = k \times t \tag{5}$$

where $k$ ($\mathrm{min}^{-1}$) is the rate constant and $t$ (min) is a time of the photocatalytic degradation.

To investigate the effect of pH on the photocatalytic degradation of the RhB dye in aqueous medium (Milli-Q water), experiments were carried out at the following pH values: 3.1, 7.4, 10.7, and 12.5. NaOH and HCl solutions were used to adjust the pH. The stability of the photocatalysts was investigated by repeating each test under the same experimental conditions. Then, the reusability of the prepared rGO@TiO$_2$/CN hybrid was investigated by recycling experiments. The photocatalytic degradation of the recycled photocatalyst was monitored using solar-like irradiation. After each cycle, the photocatalysts were collected through centrifugation, washed with absolute ethanol and Milli-Q water, and dried in the oven at 70 °C before reuse. The set-up parameters of performed photocatalytic tests are shown in Table 5.

**Table 5.** Set up of measurement parameters of the photocatalytic test.

| Parameters | Values |
|---|---|
| Catalyst concentration | 0.5 mg/mL |
| Reaction temperature | 22.0 ± 0.5 °C |
| Radiation source | Solar-like |
| Stirring rate | 350 rpm |
| Distance of light source-reactor | 15 cm |
| Radiation intensity | 64 mW/cm$^2$ |

## 4. Conclusions

In the framework of this work, the photocatalytic activity of prepared TiO$_2$ nanoparticles, TiO$_2$/rGO and TiO$_2$/CN nanocomposites, and the rGO@TiO$_2$/CN hybrid material was monitored by the photodegradation of rhodamine B (RhB) dye. Under solar light irradiation, the highest photocatalytic efficiency was obtained with the hybrid rGO@TiO$_2$/CN nanocomposite. Lower band gap energy was obtained for the hybrid rGO@TiO$_2$/CN nanocomposite. Therefore, the photocatalytic efficiency of the photocatalytic degradation of RhB dye by the hybrid rGO@TiO$_2$/g-C$_3$N$_4$ nanocomposite at different pH values and different water environment matrices (Milli-Q water, tap water, and Alkaline water) was investigated.

It was found that the photocatalytic degradation rate of RhB dye with the hybrid rGO@TiO$_2$/CN nanocomposite increased by increasing pH values. For the investigated water environment matrix, the first-order rate constant ($k$) and photocatalytic degradation efficiency ($\eta$) decreases in the following order: Milli-Q water > alkaline water > tap water.

After three repetitions of photocatalytic RhB degradation, the photodegradation efficiency of RhB decreased from 97.2% (first cycle) to 82.3% (third cycle). These results

confirmed that the hybrid rGO@TiO$_2$/CN nanocomposite can be recycled in aqueous medium, preserving its activity up to three consecutive cycles. All the demonstrated reaction mechanisms are easily scalable, and since the material used is also cheap, the explored process facilitates easy implementation into different applications.

**Author Contributions:** Conceptualization, M.K., L.Ć. and M.P.; methodology, M.K., L.Ć., M.P.; software, M.K. and T.R.; validation, M.K., L.Ć., T.R. and M.P.; formal analysis, M.K.; investigation, M.K.; resources, M.P.; data curation, M.K.; writing—original draft preparation, M.K. and T.R.; writing—review and editing, L.Ć. and M.P.; visualization, M.K., L.Ć., T.R. and M.P.; supervision, L.Ć.; project administration, M.P.; funding acquisition, L.Ć., M.P. All authors have read and agreed to the published version of the manuscript.

**Conflicts of Interest:** The authors declare no conflict of interest.

## References

1. Mathon, B.; Ferreol, M.; Coquery, M.; Choubert, J.M.; Chovelon, J.M.; Miège, C. Direct photodegradation of 36 organic micropollutants under simulated solar radiation: Comparison with free-water surface constructed wetland and influence of chemical structure. *J. Hazard. Mater.* **2021**, *407*, 124801. [CrossRef] [PubMed]
2. Oladoja, N.A.; Unuabonah, I.E. The pathways of microplastics contamination in raw and drinking water. *J. Water Process Eng.* **2021**, *41*, 102073. [CrossRef]
3. Pedrosa, M.; Figueiredo, J.L.; Silva, A.M.T. Graphene-based catalytic membranes for water treatment—A review. *J. Environ. Chem. Eng.* **2021**, *9*, 104930. [CrossRef]
4. Andreozzi, R.; Caprio, V.; Insola, A.; Marotta, R. Advanced oxidation processes (AOP) for water purification and recovery. *Catal. Today* **1999**, *53*, 51–59. [CrossRef]
5. Lin, P.; Hu, H.; Lv, H.; Ding, Z.; Xu, L.; Qian, D.; Wang, P.; Pan, J.; Li, C.; Cui, C. Hybrid reduced graphene oxide/TiO$_2$/graphitic carbon nitride composites with improved photocatalytic activity for organic pollutant degradation. *Appl. Phys. A Mater. Sci. Process.* **2018**, *124*, 510. [CrossRef]
6. Rej, S.; Bisetto, M.; Naldoni, A.; Fornasiero, P. Well-defined Cu$_2$O photocatalysts for solar fuels and chemicals. *J. Mater. Chem. A* **2021**, *9*, 5915–5951. [CrossRef]
7. Assadi, M.H.N.; Hanaor, D.A.H. The effects of copper doping on photocatalytic activity at (101) planes of anatase TiO$_2$: A theoretical study. *Appl. Surf. Sci.* **2016**, *387*, 682–689. [CrossRef]
8. Doustkhah, E.; Assadi, M.H.N.; Komaguchi, K.; Tsunoji, N.; Esmat, M.; Fukata, N.; Tomita, O.; Abe, R.; Ohtani, B.; Ide, Y. In situ Blue titania via band shape engineering for exceptional solar H$_2$ production in rutile TiO$_2$. *Appl. Catal. B Environ.* **2021**, *297*, 120380. [CrossRef]
9. Shehzad, N.; Tahir, M.; Johari, K.; Murugesan, T.; Hussain, M. A critical review on TiO$_2$ based photocatalytic CO$_2$ reduction system: Strategies to improve efficiency. *J. CO$_2$ Util.* **2018**, *26*, 98–122. [CrossRef]
10. Ma, L.; Jia, I.; Guo, X.; Xiang, L. High performance of Pd catalysts on bimodal mesopore for the silica catalytic oxidation of toluene. *Chin. J. Catal.* **2014**, *35*, 108–119. [CrossRef]
11. Gao, H.; Zhang, P.; Hu, J.; Pan, J.; Fan, J.; Shao, G. One-dimensional Z-scheme TiO$_2$/WO$_3$/Pt heterostructures for enhanced hydrogen generation. *Appl. Surf. Sci.* **2017**, *391*, 211–217. [CrossRef]
12. Das, S.; Mahalingam, H. Exploring the synergistic interactions of TiO$_2$, rGO, and *g*-C$_3$N$_4$ catalyst admixtures in a polystyrene nanocomposite photocatalytic film for wastewater treatment: Unary, binary and ternary systems. *J. Environ. Chem. Eng.* **2019**, *7*, 103246. [CrossRef]
13. Ibrahim, Y.O.; Hezam, A.; Qahtan, T.F.; Al-Aswad, A.H.; Gondal, M.A.; Drmosh, Q.A. Laser-assisted synthesis of Z-scheme TiO$_2$/rGO/*g*-C$_3$N$_4$ nanocomposites for highly enhanced photocatalytic hydrogen evolution. *Appl. Surf. Sci.* **2020**, *534*, 147578. [CrossRef]
14. Allen, J.M.; Vincent, T.C.; Richard, K.B. Honeycomb carbon: A Review of Graphene What is graphene? *Chem. Rev.* **2010**, *110*, 132–145. [CrossRef] [PubMed]
15. Erickson, K.; Erni, R.; Lee, Z.; Alem, N.; Gannett, W.; Zettl, A. Determination of the local chemical structure of graphene oxide and reduced graphene oxide. *Adv. Mater.* **2010**, *22*, 4467–4472. [CrossRef]
16. Kovačić, M.; Perović, K.; Papac, J.; Tomić, A.; Matoh, L.; Žener, B.; Brodar, T.; Capan, I.; Surca, A.K.; Kušić, H.; et al. One-Pot Synthesis of Sulfur-Doped TiO$_2$/Reduced Graphene Oxide Composite (S-TiO$_2$/rGO) with Improved Photocatalytic Activity for the Removal of Diclofenac from Water. *Materials* **2020**, *13*, 1621. [CrossRef]

17. Zouzelka, R.; Remzova, M.; Plsek, J.; Brabec, L.; Rathousky, J. Immobilized rGO/TiO$_2$ photocatalyst for decontamination of water. *Catalysts* **2019**, *9*, 708. [CrossRef]

18. Kocijan, M.; Ćurković, L.; Ljubas, D.; Mužina, K.; Bačić, I.; Radošević, T.; Podlogar, M.; Bdikin, I.; Otero-Irurueta, G.; Hortigüela, M.J.; et al. Graphene-Based TiO$_2$ Nanocomposite for Photocatalytic Degradation of Dyes in Aqueous Solution under Solar-Like Radiation. *Appl. Sci.* **2021**, *11*, 3966. [CrossRef]

19. Kusiak-Nejman, E.; Wanag, A.; Kapica-Kozar, J.; Kowalczyk, Ł.; Zgrzebnicki, M.; Tryba, B.; Przepiórski, J.; Morawski, A.W. Methylene blue decomposition on TiO$_2$/reduced graphene oxide hybrid photocatalysts obtained by a two-step hydrothermal and calcination synthesis. *Catal. Today* **2019**, *357*, 630–637. [CrossRef]

20. Bairamis, F.; Konstantinou, I.; Petrakis, D.; Vaimakis, T. Enhanced Performance of Electrospun Nanofibrous TiO$_2$/$g$-C$_3$N$_4$ Photocatalyst in Photocatalytic Degradation of Methylene Blue. *Catalysts* **2019**, *9*, 880. [CrossRef]

21. Rusek, J.; Paušová, Š.; Praus, P.; Krýsa, J. Immobilization of Exfoliated $g$-C$_3$N$_4$ for Photocatalytical Removal of Organic Pollutants from Water. *Catalysts* **2021**, *11*, 203. [CrossRef]

22. Starukh, H.; Praus, P. Doping of graphitic carbon nitride with non-metal elements and its applications in photocatalysis. *Catalysts* **2020**, *10*, 1119. [CrossRef]

23. Wang, J.; Sun, Y.; Fu, L.; Sun, Z.; Ou, M.; Zhao, S.; Chen, Y.; Yu, F.; Wu, Y. A defective $g$-C$_3$N$_4$/RGO/TiO$_2$composite from hydrogen treatment for enhanced visible-light photocatalytic H2production. *Nanoscale* **2020**, *12*, 22030–22035. [CrossRef] [PubMed]

24. Li, W.; Chen, Q.; Zhong, Q. One-pot fabrication of mesoporous $g$-C$_3$N$_4$/NiS co-catalyst counter electrodes for quantum-dot-sensitized solar cells. *J. Mater. Sci.* **2020**, *55*, 10712–10724. [CrossRef]

25. Thirumalraj, B.; Rajkumar, C.; Chen, S.M.; Palanisamy, S. One-Pot Green Synthesis of Graphene Nanosheets Encapsulated Gold Nanoparticles for Sensitive and Selective Detection of Dopamine. *Sci. Rep.* **2017**, *7*, 41213. [CrossRef] [PubMed]

26. An, T.; Tang, J.; Zhang, Y.; Quan, Y.; Gong, X.; Al-Enizi, A.M.; Elzatahry, A.A.; Zhang, L.; Zheng, G. Photoelectrochemical Conversion from Graphitic C$_3$N$_4$ Quantum Dot Decorated Semiconductor Nanowires. *ACS Appl. Mater. Interfaces* **2016**, *8*, 12772–12779. [CrossRef]

27. Kang, Y.; Yang, Y.; Yin, L.C.; Kang, X.; Liu, G.; Cheng, H.M. An Amorphous Carbon Nitride Photocatalyst with Greatly Extended Visible-Light-Responsive Range for Photocatalytic Hydrogen Generation. *Adv. Mater.* **2015**, *27*, 4572–4577. [CrossRef]

28. Choi, Y.-J.; Kim, E.; Han, J.; Kim, J.-H.; Gurunathan, S. A Novel Biomolecule-Mediated Reduction of Graphene Oxide: A Multifunctional Anti-Cancer Agent. *Molecules* **2016**, *21*, 375. [CrossRef]

29. Hu, L.; Flanders, P.M.; Miller, P.L.; Strathmann, T.J. Oxidation of sulfamethoxazole and related antimicrobial agents by TiO$_2$ photocatalysis. *Water Res.* **2007**, *41*, 2612–2626. [CrossRef]

30. Hafeez, H.Y.; Lakhera, S.K.; Bellamkonda, S.; Rao, G.R.; Shankar, M.V.; Bahnemann, D.W.; Neppolian, B. Construction of ternary hybrid layered reduced graphene oxide supported $g$-C$_3$N$_4$-TiO$_2$ nanocomposite and its photocatalytic hydrogen production activity. *Int. J. Hydrog. Energy* **2018**, *43*, 3892–3904. [CrossRef]

31. Ali, M.H.H.; Al-Afify, A.D.; Goher, M.E. Preparation and characterization of graphene–TiO$_2$ nanocomposite for enhanced photodegradation of Rhodamine-B dye. *Egypt. J. Aquat. Res.* **2018**, *44*, 263–270. [CrossRef]

32. Maruthamani, D.; Divakar, D.; Kumaravel, M. Enhanced photocatalytic activity of TiO$_2$ by reduced graphene oxide in mineralization of Rhodamine B dye. *J. Ind. Eng. Chem.* **2015**, *30*, 33–43. [CrossRef]

33. Dharwadkar, S.; Yu, L.; Achari, G. Photocatalytic degradation of sulfolane using a led-based photocatalytic treatment system. *Catalysts* **2021**, *11*, 624. [CrossRef]

34. Ćurković, L.; Ljubas, D.; Šegota, S.; Bačić, I. Photocatalytic degradation of Lissamine Green B dye by using nanostructured sol-gel TiO$_2$ films. *J. Alloys Compd.* **2014**, *604*, 309–316. [CrossRef]

35. Fagan, R.; McCormack, D.E.; Hinder, S.J.; Pillai, S.C. Photocatalytic properties of $g$-C$_3$N$_4$-TiO$_2$ heterojunctions under UV and visible light conditions. *Materials* **2016**, *9*, 286. [CrossRef]

36. Alharthi, F.A.; Ali Alghamdi, A.; Alanazi, H.S.; Alsyahi, A.A.; Ahmad, N. Photocatalytic Degradation of the Light Sensitive Organic Dyes: Methylene Blue and Rose Bengal by Using Urea Derived $g$-C$_3$N$_4$/ZnO Nanocomposites. *Catalysts* **2020**, *10*, 1457. [CrossRef]